



1 **Investigating the spatiotemporal features of glacier**
2 **elevation changes over the southeastern Tibetan Plateau**
3 **using multisource satellite data**

4 Xin Luo¹, Hongping Zeng², Zhen Ye³

5 ¹ School of Earth Sciences, Yunnan University, Kunming, 650500, China

6 ² Institute of International Rivers and Eco-security, Yunnan University, Kunming, 650500, China

7 ³ College of Surveying and Geoinformatics, Tongji University, Shanghai, 200092, China

8 *Correspondence to:* Xin Luo (xinluo_xin@ynu.edu.cn)

9 **ABSTRACT.** Glaciers in the southeastern Tibetan Plateau (SETP) feature the largest maritime glaciers
10 on the Tibetan Plateau (TP) and have experienced accelerated melting in recent decades. Investigating
11 the spatiotemporal features of glacier elevation changes in the SETP remains a challenging task since
12 this region is highly heterogeneous and high spatiotemporal resolution observations for region-wide
13 glacier change measurements are still insufficient. To better understand the spatiotemporal variations in
14 glacier elevation changes in the SETP, multisource satellite observations, including ASTER DEM,
15 ICESat, ICESat-2 and CryoSat-2, are integrated in this study. We derive the spatially resolved glacier
16 change for each year based on the $0.5^\circ \times 0.5^\circ$ geographical tiles, and the obtained glacier elevation
17 change rate of the entire SETP is $-0.710 \pm 0.046 \text{ m/yr}$ during 2000–2022. We divided the study
18 period into a recent decade and the previous decade and found that glacier thinning accelerated at a rate
19 of 31.2% in the recent decade. We evaluated the correlation between the elevation measurements of
20 different satellites and found that the elevation measurement of ICESat-2 had a slight negative bias
21 relative to the measurements of the other satellites. The ICESat-2 elevation measurements of the strong
22 beam and weak beam were also compared, and no significant difference was observed. We also compared
23 the CryoSat-2 swath measurements with the Level-2 (L2) measurements, and we found that the CryoSat-
24 2 swath data agreed significantly more with the other satellite data than with the L2 measurements. A
25 comprehensive comparison is carried out for the glacier elevation changes obtained in existing studies.
26 Our estimates are highly consistent with those of new published studies and have a finer temporal scale
27 and less estimation uncertainty.



28 **Keywords:** Southeastern Tibetan Plateau, glacier elevation change, ASTER stereo images, ICESAT data,
29 CryoSat-2.

30 1 Introduction

31 Glaciers are sensitive to climate change (Bach et al., 2018; Yao et al., 2012), and most of the world's
32 glaciers, excluding the Greenland and Antarctic ice sheets, have experienced accelerated ice melting and
33 mass loss in recent decades (Hugonnet et al., 2021; IPCC, 2020). As one of the most climate-sensitive
34 constituents of the natural landscape, glacier changes have raised broad concerns, such as contributions
35 to river and sea-level rise changes (Gardner et al., 2013; Jacob et al., 2012), sustainable water resource
36 supplies for downstream humans (Milner et al., 2017), and hazards such as glacier lake outburst floods
37 (Bolch et al., 2008; Carrivick and Tweed, 2016).

38 The High Mountain Asia (HMA) region hosts the largest glacier concentration outside the polar regions,
39 and these glaciers prominently contribute to streamflow in one of the most populated areas of the world
40 (Brun et al., 2017). Current studies have revealed that the glaciers in HMA are greatly retreating (Brun
41 et al., 2017; Gardner et al., 2013; Yao et al., 2012). Brun et al. (2017) illustrated that the glacier elevation
42 change rate for the total HMA region was -0.21 ± 0.05 m/yr during 2000-2016. Shean et al. (2020)
43 revealed that the total HMA glacier mass change rate during 2000-2018 was -0.19 ± 0.03 m w.e./yr.
44 Glacier elevation change shows large spatial variability in HMA; that is, Shen et al. (2020) illustrated a
45 positive glacier elevation change rate of 0.047 ± 0.06 m/yr in Kunlun for 2000-2018 (Shean et al.,
46 2020). Kääb et al. (2015) illustrated that a slight negative glacier elevation change rate of -0.1 ± 0.06 m/yr
47 was observed in Karakoram for 2003-2008 (Kääb et al., 2015), and Brun et al. (2017) illustrated that the
48 most negative elevation change rate of -0.73 ± 0.27 m/yr was found in Nyainqentanglha for 2000-2016.
49 Among the subregions of the HMA region, the SETP has experienced dramatic glacier mass loss over
50 the past two decades; however, the glacier elevation changes in the SETP have not been well quantified
51 by existing studies due to inconsistent results. For example, the Nyainqentanglha region (the main SETP)
52 was reported to experience a very negative elevation change rate of -1.34 ± 0.29 m yr⁻¹ from 2003–2008
53 according to Kääb et al. (2015), while a slight negative change rate of approximately -0.30 ± 0.13 m/yr
54 ¹ from 2003–2008 was revealed by Gardner et al. (2013). According to in situ and remotely sensed



55 observations, the glaciers in the SETP region have experienced the strongest recession in HMA since the
56 2000s, and this recession in the SETP accounts for approximately one-quarter to one-third of the total
57 glacier mass loss in HMA (Brun et al., 2017; Kääb et al., 2015; Neckel et al., 2014). Glacier elevation
58 changes in the SETP have drawn the most attention from glaciologists, climatologists, and geoscientists,
59 and great efforts have been made to improve elevation change estimations (Brun et al., 2017; Gardner et
60 al., 2013; Shean et al., 2020). However, estimates of glacier elevation changes are still limited in accuracy
61 and are inconsistent with each other for the SETP region. For example, various estimates of $-0.40 \pm$
62 0.41 m/yr for 2003–2009 (Gardner et al., 2013), -0.81 ± 0.32 m/yr for 2003–2008 (Neckel et al., 2014),
63 -0.68 ± 0.22 m/yr for 2000–2016 (Brun et al., 2017), -1.11 ± 0.11 m/yr for 2010–2019 (Jakob et al.,
64 2021), -0.54 ± 0.16 m/yr for 2000–2018 (Shean et al., 2020), -0.69 ± 0.35 m/yr for 2000–2019
65 (Hugonnet et al., 2021), and -0.73 ± 0.18 m/yr for 2003–2020 (Zhao et al., 2022) have been reported in
66 existing studies.

67 Glacier observations are mainly obtained through spaceborne remote sensing. There are four major
68 approaches for observing glaciers: 1) Satellite images: These images have long been used for glacier
69 observation and have provided abundant historical glacier change information along with climate change
70 information (Ke et al., 2015). Mountain glaciers can typically be automatically or semiautomatically
71 delineated with satellite images, such as Landsat, Advanced Spaceborne Thermal Emission and
72 Reflection Radiometer (ASTER), Sentinel-2, or Sentinel-1 images (Pope and Rees, 2014, Robson et al.,
73 2020; Zhou and Zhen, 2017; Peng et al., 2023). Satellite-based optical stereo images, such as ASTER
74 stereo images, WorldView stereo image, and Corona KH-4A stereo images, can be used to determine
75 glacier elevations (Shean et al., 2020; Wang et al., 2021; Muhammad and Tian, 2020; Zhao et al., 2022;
76 King et al., 2023; Piermattei et al., 2023; Ghuffar et al., 2022). 2) Geodetic digital elevation model (DEM)
77 differencing: DEM differencing is the most common approach for calculating the elevation change in an
78 entire glacier area and enables the estimation of glacier mass change over time (Cogley et al., 2011;
79 Robson et al., 2022). Generally, spaceborne optical and radar sensors are two main sources for producing
80 DEMs for calculating elevation changes in large-scale glacierized regions. Spaceborne radar DEMs, such
81 as those from the Shuttle Radar Topography Mission (SRTM) C-band data and TanDEM X-band data
82 (Ke et al., 2020; Guan et al., 2022), are generated using interferometric synthetic aperture radar (InSAR).



83 The radar signal penetrates snow and ice, and the penetration depth is a matter of debate and leads to
84 uncertainty in glacier elevation estimation (Barundun et al., 2015; Kääb et al., 2015). Spaceborne optical
85 digital models (DEMs) are generated using stereo images (Bhushan et al., 2021; King et al., 2023); the
86 generated DEMs are free of ice/snow penetration, while optical stereo images are unavailable in cloudy
87 regions. 3) Satellite altimetry. The Ice, Cloud, and Land Elevation Satellite (ICESat) missions from 2003
88 to 2009 and the following ICESat-2 mission launched in 2018 have created nearly global datasets that
89 have been widely used for glacier elevation change estimation (Zwally et al., 2002; Smith et al., 2020).
90 Additionally, the repeat cycle of CryoSat-2 has recently been exploited for glacier elevation change
91 monitoring (Zhao et al., 2022). Satellite altimetry has been an efficient approach for investigating glacier
92 elevation changes due to the continuous temporal observation of the Earth's surface; however, this
93 approach is subject to sparse spatial sampling at low latitudes, and the precision of measurement is
94 usually limited in complex terrains (Treichler et al., 2016). 4) Satellite gravity. The Gravity Recovery
95 and Climate Experiment (GRACE) satellites can be used to detect glacier change-derived variations in
96 Earth's gravity field. The GRACE estimates have very coarse spatial resolution (~150 km) and are
97 usually contaminated by water storage changes in adjacent regions; therefore, hydrological observation
98 is needed to cooperate with the determination of glacier changes when using satellite gravity (Chen et
99 al., 2017; Yi et al., 2020). Above all, a variety of data have been explored for glacier elevation changes
100 monitoring, and different data sources have respective advantages and limitations; therefore, recent
101 studies have explored the integration of multisource data to improve the precision of glacier monitoring
102 (Zhao et al., 2022; Ke et al., 2020; Muhammad and Tian, 2020; Bhattacharya et al., 2023).

103 Existing studies tend to focus on large-scale glacier elevation change monitoring, e.g., for the whole
104 HMA region or at the global scale (Brun et al., 2017; Hugonnet et al., 2021). These studies revealed that
105 the SETP has undergone accelerated glacier melting in recent years; however, the detailed spatiotemporal
106 variability in the glacier change rate remains poorly understood. In this study, we integrated multisource
107 satellite data to enhance the estimate of glacier elevation change in the SETP during the period 2000–
108 2022. Specifically, ASTER stereo images were used to generate time-series DEM data, and the generated
109 DEMs were then combined with altimetry data (including ICESat, ICESat-2 and CryoSat-2) to
110 investigate the spatiotemporal features of glacier elevation changes in the SETP. The major methods of



111 this study included the following steps: 1) We fully exploited the ASTER stereo image, ICESat, ICESat-
112 2 and CryoSat-2 altimetry data to improve the estimation of glacier elevation change. 2) We investigated
113 the spatiotemporal features of glacier elevation changes in the SETP and better quantified the
114 heterogeneity of glacier elevation changes in this region. 3) Comprehensive cross-analysis was
115 performed for elevation measurements taken by multisource satellites, as well as estimates of glacier
116 elevation changes obtained from existing studies. The remainder of this paper is structured as follows.
117 Section 2 introduces the study area and dataset. Section 3 describes the methodology. Section 4 provides
118 the results and illustrates the variations in glacier elevation change in the SETP. In Section 5, elevation
119 measurements from different satellites and estimates of glacier elevation changes from existing studies
120 are discussed. Finally, we draw conclusions in Section 6.

121 2 Study area and data

122 2.1 Study area

123 The SETP is a broad mountainous area that covers the Western Hengduan Mountains, the Eastern
124 Nyainqentanglha Ranges, and the Eastern Himalayas; the SETP boundary defined by Zhao et al. (2022)
125 was used in our study (Fig. 1). This region is characterized by complex terrain and climate. The SETP
126 has an average elevation of more than 4000 m above sea level (a.s.l.), and the mean elevation generally
127 decreases from the inner high-elevation plateau in the northwest to the southern border. According to the
128 Randolph Glacier Inventory (RGI 6.0) (RGI Consortium, 2017), the SETP hosts many glaciers, with a
129 total of 7756 glaciers and a total area of 7260 km². Among these glaciers, 301 glaciers have an area > 4
130 km² and account for approximately 50% (3638 km²) of the total glacier area. In the context of global
131 climate warming, glaciers in the SETP have been shrinking dramatically, which has caused the formation
132 of numerous glacial lakes in this region (Zhao et al., 2022; Ke et al., 2020). The mean annual temperature
133 in the SETP generally decreases from southeast to northwest. According to historical meteorological data,
134 the temperature in the SETP generally ranges from 0 °C to 19 °C, and the hottest and coldest months
135 are July and January, respectively (Prefecture, 2014). The SETP is affected by the Indian summer
136 monsoon, the East Asian summer monsoon, and westerlies, which cause the SETP to be one of the most
137 humid regions across the TP. Precipitation is mostly concentrated from April to September and accounts



138 for nearly 80% of the annual precipitation in the SETP (Zhao et al., 2022). The seasonality of
139 precipitation also varies across the region. The southern areas around the Great Bend of Yarlung Tsangpo
140 are strongly affected by the southeast monsoon, while the high-elevation mountain ranges in the northeast
141 and northwest are less impacted, resulting in a marked decrease in the mean annual precipitation from
142 the southwest to the northeast and northwest (Sakai et al., 2015).

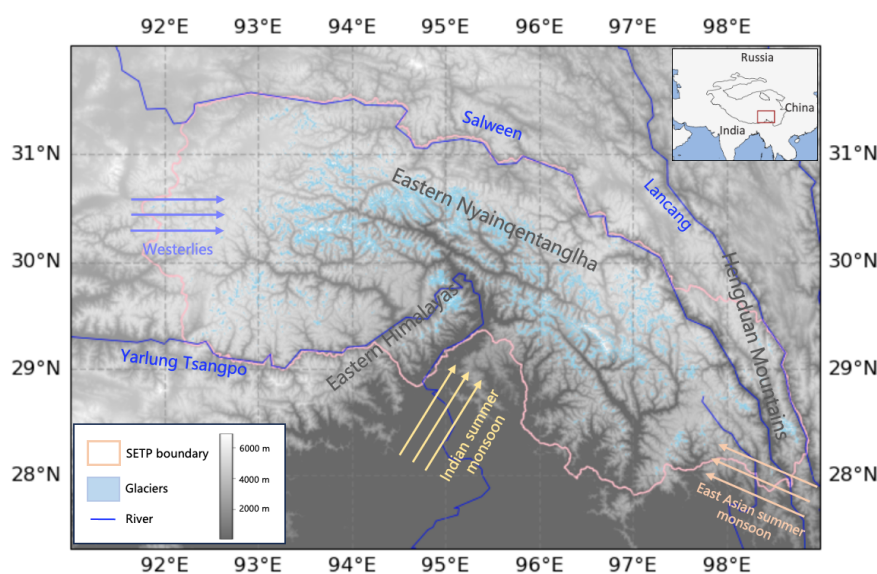


Figure 1: Overview of the SETP and the distribution of the glaciers.

143 2.2 Dataset

144 2.2.1 ASTER stereo imagery

145 The Advanced Spaceborne Thermal Emission and Reflection Radiometer (ASTER; Farr et al., 2007) is
146 an imaging instrument onboard the Terra satellite that was launched in December 1999. The ASTER
147 sensor captures high-resolution (15 to 90 m per pixel) images at a temporal resolution of 16 days with
148 fourteen different bands. Since ASTER can obtain quasireal-time (approximately 55 s difference) stereo
149 image pairs, it can produce detailed digital terrain models using the digital photogrammetry technique.
150 In this study, daytime Level-1A (L1A) stereo images (NASA/METI/AIST/Japan Spacesystems and
151 U.S./Japan ASTER Science Team, 2001) with less than 60% cloud coverage were acquired for time-
152 series DEM generation within the period 2000-2022.



153 **2.2.2 ICESat/ICESat-2 data**

154 The Ice, Cloud, and Land Elevation Satellite (ICESat) is a National Aeronautics and Space
155 Administration (NASA) satellite mission for measuring ice sheet mass balance, cloud and aerosol heights,
156 land topography and vegetation characteristics. ICESat carries the Geoscience Laser Radar Altimeter
157 System (GLAS) and emits infrared and visible laser pulses at 1064- and 532-nm wavelengths with a
158 revisit cycle of 91 days. The Ice, Cloud, and Land Elevation Satellite-2 (ICESat-2) is the second
159 generation of the laser altimeter ICESat mission. ICESat-2 was launched in 2018 and carries the
160 Advanced Topographic Laser Altimeter System (ATLAS) instrument for land elevation measurements.
161 ATLAS emits visible laser pulses at a wavelength of 532 nm, and it generates six beams arranged in
162 three pairs that enable increased coverage of the Earth's surface compared to that of its predecessor,
163 ICESat, which has only one laser beam. In this study, ICESat/GLAH14 data (Zwally et al., 2014) from
164 2003-2009 and ICESat-2/ALT06 data (Smith et al., 2020) from 2018-2022 were collected through the
165 National Snow & Ice Data Center (NSIDC).

166 **2.2.3 CryoTEMPO EOLIS data**

167 The EOLIS (Elevation Over Land Ice from Swath) is part of the European Space Agency (ESA) CryoSat-
168 2 thematic product (CryoTEMPO, Gourmelen et al., 2018), which aims to extend the ability of CryoSat-
169 2 to measure elevation changes in areas of sea ice, polar oceans, land ice, coastal areas, and hydrology.
170 The EOLIS products exploit Swath processing of CryoSat's SARIn mode, which makes full use of the
171 information contained in CryoSat-2's waveforms and provides data with increased spatial and temporal
172 coverage over land ice (Gourmelen et al., 2018). The CryoTEMPO EOLIS consists of two distinct
173 products: a point product containing a cloud of elevations with associated uncertainty in geospatial units
174 and a gridded product containing a spatial interpolation of the point product onto a uniform grid of
175 elevation and uncertainty. The CryoTEMPO-EOLIS point product and gridded product are produced for
176 14 geographic regions of the Earth. Due to the lack of data available for the SETP region, CryoTEMPO
177 EOLIS point data were collected for our study. Specifically, the CryoTEMPO EOLIS point data provide
178 a monthly elevation dataset with associated uncertainties in 100×100 km geospatial tiles and temporal
179 coverage from July 2010 until now. We collected the CryoTEMPO-EOLIS point data in the temporal



180 range from July 2010 to December 2022 in our study, and the data were obtained from <https://cryotempo->
181 [eolis.org](https://cryotempo-eolis.org).

182 **2.2.4 Ancillary datasets**

183 The high-resolution DEMs generated from NASA's Shuttle Radar Topography Mission (SRTM; Farr et
184 al., 2007) in 2000 were acquired in our study. Specifically, we selected the void-filled version of the
185 SRTM-GL1 DEM to assist in ASTER DEM generation and time-series elevation change calculations.
186 To generate the surface water masked DEM image, the Global Surface Water (GSW) dataset derived
187 from the European Commission's Joint Research Centre (JRC) was collected (Pekel et al., 2016).
188 Moreover, the GlobeLand30 land cover dataset (Chen et al., 2015) from 2010 was acquired to determine
189 the stable region of the SETP, and the Randolph Glacier Inventory (RGI 6.0) outlines were used to
190 identify the glacier region in our study (RGI Consortium, 2017).

191 **3 Methodology**

192 **3.1 Time-series DEM generation from ASTER stereo imagery**

193 We used the Ames Stereo Pipeline (Beyer et al., 2018; Shean et al., 2016) tool to create time-series
194 ASTER DEMs instead of acquiring existing DEM datasets online. The time-series DEM is generated
195 based on automatic processing with ASTER Level 1A stereo images. Specifically, we processed the
196 ASTER pairs using the void-filled SRTM-GL1 DEM as a seed DEM for initial orthorectification. The
197 semiglobal matching (SGM) algorithm (Hirschmuller, 2008) with a kernel size of 9×9 pixels was used
198 for stereo matching, and the ternary census transform was selected as the cost function (Han et al., 2016).
199 Subpixel refinement was also implemented to improve stereo matching; specifically, affine window
200 adaptation with a kernel size of 25×25 pixels was applied to obtain subpixel disparities. The generated
201 DEM contains serious errors due to inaccurate stereo matching of the complex landscape or cloud
202 contamination of the image; then, we removed the outlier elevation pixels with heights that differed by
203 more than 150 m from the SRTM-GL1 DEM. To generate yearly ASTER DEMs, image mosaicing
204 processing was carried out for all the generated DEMs of each year to eliminate the holes in the generated
205 DEM image. To avoid seasonal effects in the time-series analysis of glacier elevation changes, the



206 generated ASTER DEMs with acquisition dates near July (glacier ablation season) were placed on the
207 top layer during the ASTER DEM mosaicking. To derive reliable glacier elevation changes based on
208 multisource elevation datasets, coregistration of the generated ASTER DEMs was carried out. We applied
209 the method proposed by Nuth and Kääb (2011) to calculate the geometrical shifts, systemic offsets, and
210 elevation-dependent biases of the generated ASTER DEMs using the SRTM-GL1 DEM as a reference.
211 The parameter for coregistration was calculated based on the ASTER DEM of the stable region, which
212 was determined by masking the glacier region, surface water region, forest region, shrub region and
213 cropland region by using RGI 6.0 data, JRC GSW data and Globeland30 data, respectively.

214 **3.2 Time-series elevation change calculation**

215 We performed multisource data processing on the geographical $0.5^\circ \times 0.5^\circ$ tiles of each year, and the
216 elevation difference between the derived elevation and SRTM-GL1 DEM data was subsequently
217 calculated for each tile and each year. Altimetry data, including ICESat, ICESat-2 and CryoSat-2 data,
218 measure surface elevation through spaceborne altimeters, and the derived elevation usually has high
219 precision (Fricker et al., 2005; Brunt et al., 2019). However, altimeter measurements are sparsely
220 distributed on the ground surface, which limits the capability of continuous earth surface monitoring.
221 Therefore, the altimetry data-based elevation difference was calculated for only the locations of altimeter
222 footprints. The obtained elevation differences had errors caused by either the satellite data measurements
223 or the SRTM DEM data. To prevent bias in the estimation of elevation change, elevation differences
224 larger than 150 m were removed from our study. We calculated the mean elevation difference for the
225 glacier region and stable region on each geographical tile. Since the glacier elevation change varied at
226 different altitudes, the mean elevation difference was calculated for each 100-m elevation bin of the
227 glacier region, except for the ICESat data-derived elevation differences, due to the limited amount of
228 measurements.

229 **3.3 Estimation of glacier elevation/mass change**

230 We derived the glacier elevation change in each graphical tile by a glacier area-weighting method based
231 on the elevation bins of the tile. To remove the systematic error between the derived elevation and SRTM
232 DEM, we corrected the glacier elevation change based on the elevation change estimate in the stable



233 region, and the correction was as follows:

$$234 \quad dh_{glacier-cor} = dh_{glacier} - dh_{stable} \quad (1)$$

235 where dh is the elevation difference between the derived elevation and SRTM DEM. We performed
236 corrections of glacier elevation changes, which were derived from satellite data from different sources
237 except for the CryoTEMP EOLIS point data since elevation measurements were lacking in the nonglacier
238 region. To remove the systematic error in elevation change obtained from CryoTEMP EOLIS data, we
239 adopted an indirect approach; that is, the changes in CryoTEMP elevation were corrected by referring to
240 the corrected elevation change in the ICESAT-2 data. Specifically, the corrected CryoTEMP elevation
241 changes are obtained by subtracting the mean difference between the elevation changes derived from the
242 CryoTEMP and ICESAT-2 data during the overlap period. The correction for the change in CryoTEMP
243 elevation is as follows:

$$244 \quad dh_{glacier-cor}^{Cryo} = dh_{glacier}^{Cryo} - \overline{(dh_{glacier}^{Cryo} - dh_{glacier}^{sat2})_{year}} \quad (2)$$

245 where $dh_{glacier-cor}^{Cryo}$ and $dh_{glacier}^{sat2}$ are the glacier elevation changes derived from CryoTEMP and
246 ICESAT-2 data, respectively. $year$ represents the overlapping year of the CryoTEMP and ICESAT-2
247 measurements. We obtained the corrected elevation change for each geographical tile, and the overall
248 elevation change for the entire SETP can be obtained with a glacier area-weighted method based on
249 geographical tiles. Accordingly, the glacier mass change can be calculated through $\Delta M = \Delta V \cdot \rho_g = A \cdot$
250 $\Delta h \cdot \rho_g$, where ΔV is the volume of the glacier change, which can be calculated by multiplying the
251 glacier area A and glacier elevation change Δh . ρ_g is the glacier density, which was set to
252 850 kg m^{-3} in our study (Brun et al., 2017).

253 3.4 Uncertainty estimation

254 The time-series elevation changes for the geographical tiles and the entire SETP region can be obtained
255 from four satellite images with different temporal coverages. To prevent large biases caused by single
256 satellite data-derived elevation changes, a simple averaging method is used for fusing multisource data-
257 derived elevation changes. To estimate the rates of glacier elevation change for each geographical tile
258 and the entire SETP region, a robust linear fitting using the random sample consensus (RANSAC)



259 algorithm was carried out for the time-series elevation changes. The uncertainty in the elevation change
260 rate can be derived from the residuals of the fitted elevation changes, and the calculation is as follows:

$$261 \quad \varepsilon = y_i - y_{fitted} \quad (3)$$

$$262 \quad \sigma_{dh} = \sqrt{\frac{1}{n} \sum_{i=1}^n (\varepsilon_i - \bar{\varepsilon})^2} \quad (4)$$

$$263 \quad \sigma_{dh/dt} = \frac{\sigma_{dh}}{dt} \quad (5)$$

264 where ε is the residual of the fitted elevation change y_{fitted} and y_i is the original elevation change
265 corresponding to the i -th year. dt and dh are the temporal coverage of the study phase and the overall
266 elevation change, respectively.

267 The uncertainty in glacier mass change can be calculated through $\sigma_{\Delta M} = \sqrt{\sigma_{\Delta M,r}^2 + \sigma_{\Delta M,s}^2}$, where $\sigma_{\Delta M,r}$
268 and $\sigma_{\Delta M,s}$ are the random error and systematic error, respectively. The random errors caused by three
269 main sources are assumed to be independent: the uncertainty in elevation change Δh , the uncertainty in
270 glacier area σ_A , and the uncertainty in glacier density σ_{ρ_g} . The uncertainty in the glacier density
271 60 kg m^{-3} was used in our study (Brun et al., 2017). Then, the random error can be calculated by:

$$272 \quad \sigma_{\Delta M,r} = \sqrt{(\sigma_{\Delta v} \cdot \rho_g)^2 + (\sigma_{\rho_g} \cdot \Delta V)^2} \quad (6)$$

273 where $\sigma_{\Delta v}$ is the uncertainty in the change in glacier volume and can be calculated by:

$$274 \quad \sigma_{\Delta v} = \sqrt{(\sigma_{\Delta h} \cdot A)^2 + (\sigma_A \cdot \Delta h)^2} \quad (7)$$

275 where σ_A is the uncertainty in the glacier area, which we set to $0.1A$ in our study (Brun et al., 2017;
276 Kääb et al., 2012). To assess the systematic error, we are inspired by Brun et al. (2017) and use the
277 absolute value of the triangulation residual between two subperiods as the systematic error:

$$278 \quad \sigma_{\Delta M,s} = |\Delta M_{2000-2022} - (\Delta M_{2000-2012} + \Delta M_{2013-2022})| \quad (8)$$

279 where $\Delta M_{xxxx-yyyy}$ is the glacier mass change for the period between $xxxx$ and $yyyy$.



280 **4 Results**

281 **4.1 Glacier elevation changes in the SETP region**

282 We derived glacier elevation changes from multisource satellite data (Fig. 2 (a)). According to the
283 average glacier elevation changes, the glaciers experienced rapid thinning with a total elevation change
284 of -16.942 ± 1.06 m during the period 2000-2022, which corresponded to the glacier mass changes
285 of -100.70 ± 13.94 Gt. We divided the period into two subperiods, 2000-2012 and 2012-2022, and the
286 glacier mass changes for the periods 2000-2012 and 2012-2022 were -46.76 ± 9.31 Gt and
287 -53.20 ± 8.21 Gt, respectively. The obtained glacier elevation changes varied between satellite data
288 sources. As shown in Table 1, even though all the satellite measurements revealed negative glacial
289 elevation changes for different periods during 2000-2022, the rates of glacier elevation change derived
290 from different satellite data showed significant differences, which demonstrated that estimation errors
291 exist among the single satellite data-derived results. We estimated the rate of glacier elevation change by
292 integrating multisource satellite data. According to Table 1, the obtained rates of glacier elevation change
293 for 2000-2022, 2000-2012, and 2013-2022 were -0.710 ± 0.046 m/yr, -0.583 ± 0.052 m/yr and
294 -0.765 ± 0.037 m/yr, respectively. The obtained rates of glacier elevation change demonstrated that
295 glacier thinning in the recent decade of 2012-2022 accelerated at a rate of 31.2% compared with that in
296 the previous decade of 2000-2012. The glacier elevation change rate also varied with altitude; as shown
297 in Fig. 2 (b), glacier melting occurred at a faster rate at reduced altitudes. Specifically, the fastest glacier
298 thinning rate was approximately -1.6 m/yr at an altitude of approximately 4000 m. When the altitude
299 increased to 4700 m, glacier thinning was maintained at a rate of approximately -0.5 m/yr until the
300 altitude reached 5400 m. When the altitude was above 5900 m, the change in glacier elevation became
301 positive.

302 Table 1. Glacier elevation change rates derived from multisource data.

Data source	Period	Elevation change rate (m/yr)
ICESAT/GLAS	2003-2009	-1.179 ± 0.440
ICESAT-2/ATL	2018-2022	-0.336 ± 0.118
CryoTEMP EOLIS	2010-2022	-1.065 ± 0.109
ASTER DEMs	2000-2022	-0.604 ± 0.296
Combined	2000-2022	-0.710 ± 0.046



2000-2012	-0.583 ± 0.052
2012-2022	-0.784 ± 0.035

303

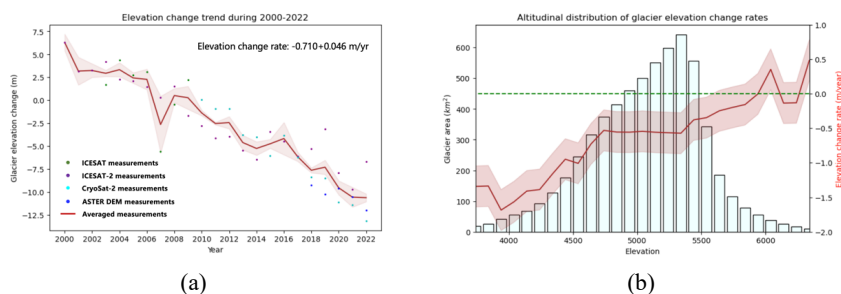


Figure 2: Temporal and altitudinal glacier elevation change in SETP. (a) Multisource satellite data-integrated glacier elevation changes during 2000-2022 and (b) the altitudinal distribution of glacier elevation change rates.

304 **4.2 Spatiotemporal variability in glacier elevation change**

305 The total glacier area in the SETP is approximately 7260 km², and most of the glaciers are distributed
 306 in the latitudinal range 29° N-31° N and the longitudinal range 93° E- 97.5° E (Fig. 2. (a)). Among
 307 the total 0.5° × 0.5° geographical tiles of the SETP, the tiles of latitude 29° N-29.5° N and longitude
 308 96.5° E-97° E cover the largest glacier area of 768 km². With a simple statistical analysis of the glacier
 309 area of tiles, 17 tiles had glacier areas larger than 100 km², and the aggregated area accounted for 83%
 310 of the total glacier area of the SETP region. Since a smaller glacier area usually corresponds to fewer
 311 satellite measurements and thus introduces great uncertainty in glacier elevation change calculations, we
 312 selected 17 geographical tiles with glacier areas larger than 100 km² for quantitative analysis in our
 313 study. According to Fig. 3 (a) and (c), the fastest glacier thinning events occurred at latitude 29° N-
 314 29.5° N and longitude 97° E-97.5° E, and the slightest glacier thinning occurred at latitudes 30° N-
 315 30.5° N and longitudes 93.5° E - 94° E, corresponding to glacier thinning rates of $-0.930 \pm$
 316 0.164 m/yr and $-0.421 \pm 0.211 \text{ m/yr}$, respectively. We further estimated the change in glacier
 317 elevation between 2000-2012 and 2012-2022. The glacier elevation change rates and their difference
 318 values for the two periods are illustrated in Fig. 3. (c) and (b), where 12 geographical tiles showed larger
 319 negative changes from 2012-2022 than from 2000-2012; in general, these findings revealed that the
 320 glaciers thinned at an accelerating rate in approximately 70% of the region in the SETP in the past decade.



321 Specifically, the glacier thinning rates were less than 1 m/yr for all the geographical tiles from 2000–
322 2012; however, in the next decade from 2012–2022, 9 geographical tiles experienced glacier thinning
323 rates higher than 1 m/yr, and the fastest glacier thinning rate reached 2.151 m/yr, which demonstrated
324 a serious accelerated glacier thinning rate in the SETP region.

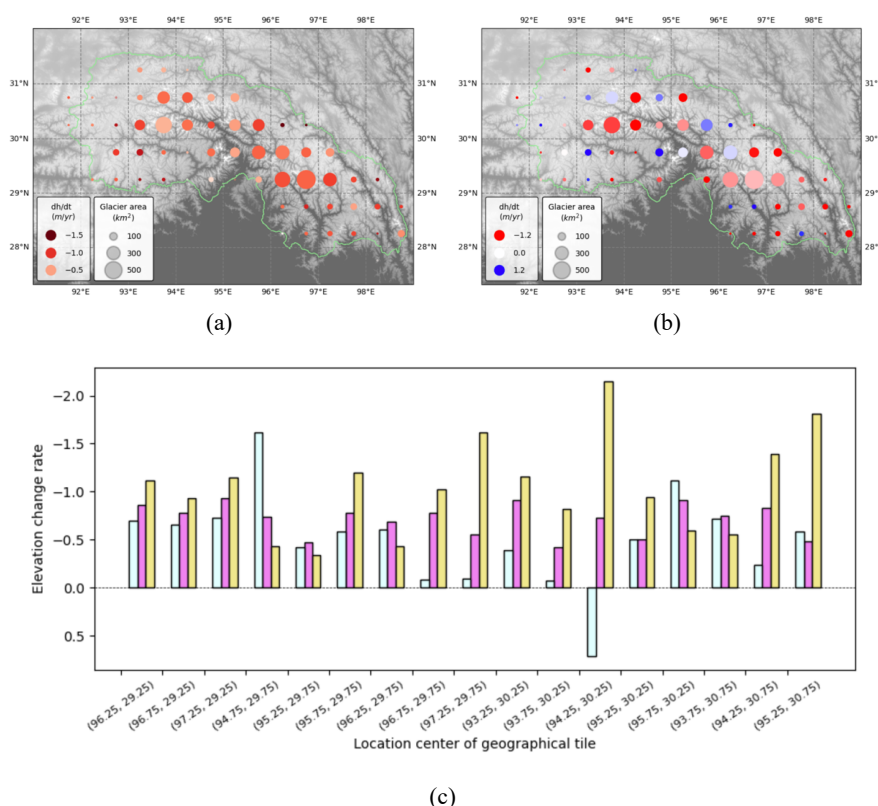


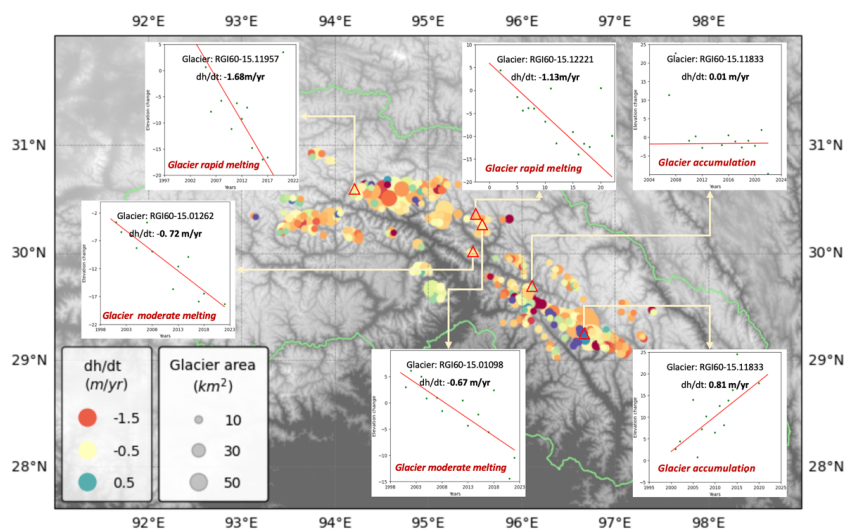
Figure 3: Spatial distribution of the glacier elevation change rate. (a) The spatial distribution of glacier elevation change rate during 2000-2022, and (b) the spatial distribution of the difference of rates of glacier elevation change between 2000-2012 and 2012-2022.

325 4.3 Individual glacier changes

326 We estimated the rate of elevation change for individual glaciers and explored the variability in the rate
327 of change in glacier elevation in the SETP. A total of 301 glaciers with areas larger than 4 km², which
328 accounted for 51% of the glacier area in the SETP, were selected for analysis in our study. As shown in
329 Fig. 4, most of the glaciers demonstrated negative elevation changes, while a small portion of the glaciers
330 still exhibited a positive elevation change during the period 2000-2022. The glacier thinning rate varies

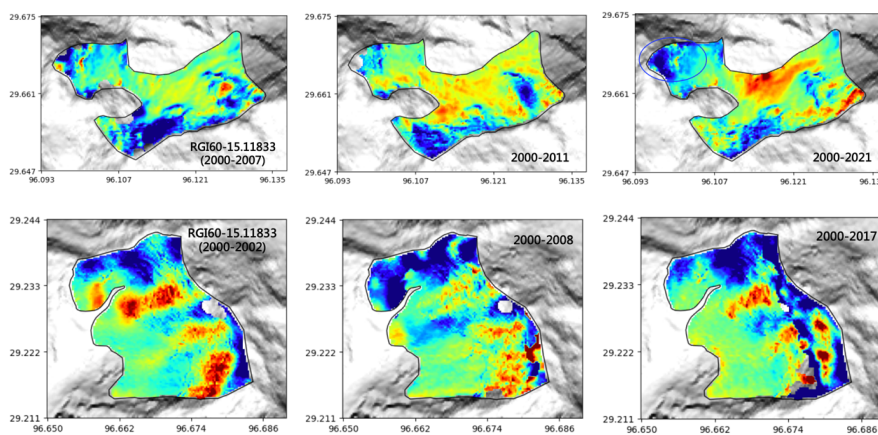


331 with spatial distribution and glacier area; to explore the features of elevation change in individual glaciers,
332 we selected individual glaciers corresponding to different elevation change ranges for further analysis.
333 Specifically, we divided the glaciers into three types, namely, regions with glacier accumulation,
334 moderate glacier thinning rate, and rapid glacier thinning rate, which corresponded to elevation change
335 rates larger than 0 m/yr, between -1 m/yr and -0 m/yr, and smaller than -1 m/yr, respectively. The glacier
336 area proportions of the three types of glaciers accounted for 12.6%, 56.5%, and 30.9%, respectively.
337 Specifically, the glaciers of RGI60-15.12221 and RGI60-15.11833 were selected for glacier
338 accumulation analysis. According to Fig. 4 (b), these two glaciers experienced positive elevation changes
339 in the context of glacier thinning trends during the period 2000-2022 in the SETP. In particular, the
340 RGI60-15.11833 glacier achieved a high glacier accumulation rate of 0.81 m/yr during the period of
341 2000-2022. According to the visualization of the two glacier accumulation cases shown in Fig. 4 (b),
342 both glacier thinning and glacier accumulation occurred, and glacier accumulation was dominant in the
343 glaciers. We selected the glaciers RGI60-15.01098 and RGI60-15.01098 for the analysis of moderate
344 glacier thinning rates. These two glaciers exhibited similar general trends of glacier elevation change,
345 and the rates of glacier elevation change were -0.67 m/yr and -0.72 m/yr, respectively. The elevation
346 change maps shown in Fig. 4 (c) illustrate that negative elevation changes were dominant in the
347 individual glaciers. In addition to having a moderate glacier thinning rate, some glaciers experienced
348 rapid negative elevation changes during the period of 2000-2022. We selected two glaciers, RGI60-
349 15.11957 and RGI60-15.12221, to represent rapid glacier thinning. The rates of glacier elevation change
350 for the two selected glaciers reached to -1.13 m/yr and -1.68 m/yr, and most regions of the individual
351 glaciers experienced severe negative elevation changes, as shown in Fig. 4 (d).

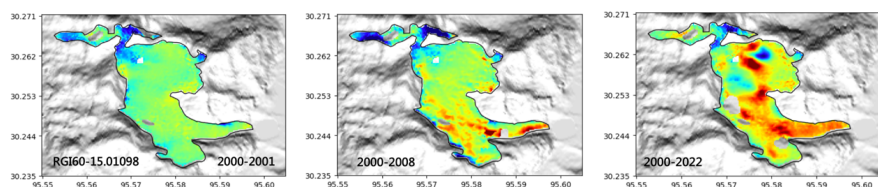


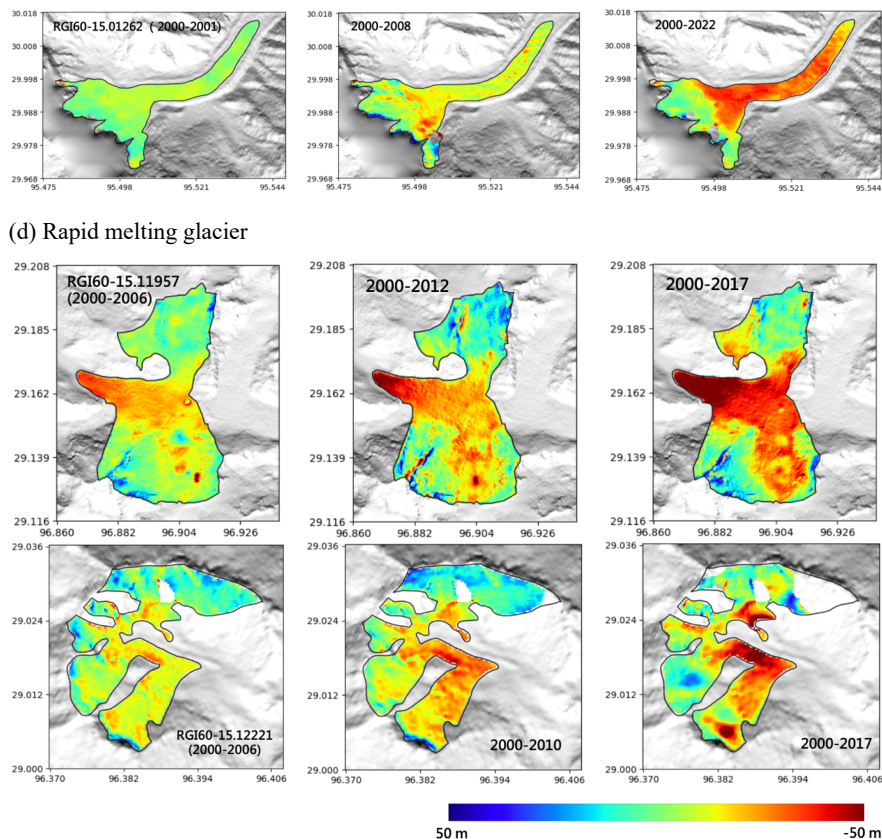
(a)

(b) Accumulated glacier



(c) Moderate melted glacier





(d) Rapid melting glacier

Figure 4: Spatial distribution and elevation change rates of individual glaciers. (a) The spatial distribution of elevation change rates for individual glaciers. (b), (c), and (d) correspond to the glacier accumulation, moderate glacier melting rate, and rapid glacier melting rate cases, respectively.

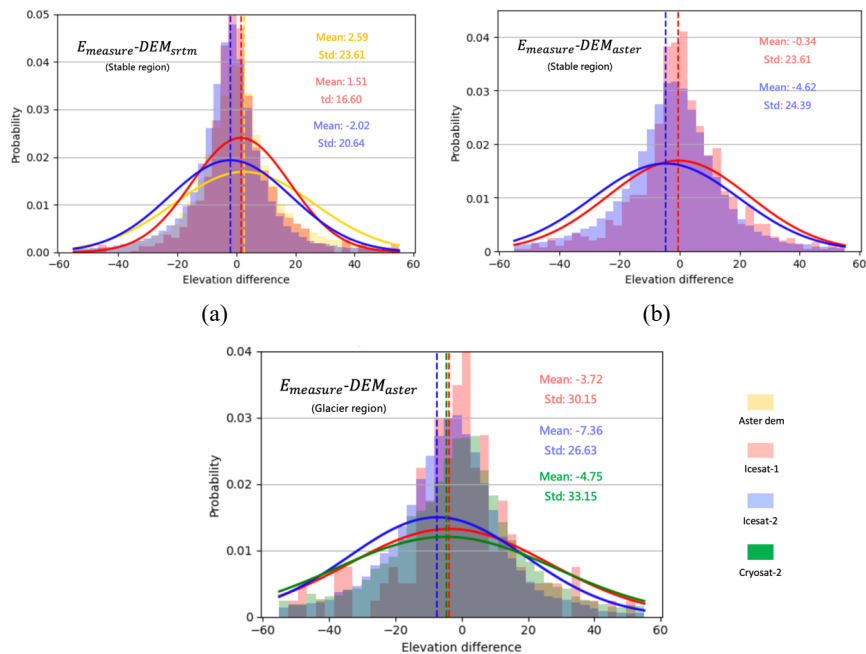
352 **5 Discussion**

353 **5.1 Cross-analysis of multisource satellite measurements**

354 We evaluated the quality of the elevation measurements through a cross-analysis of the results derived
355 from different satellite sources. We assumed that the error of the DEM was spatially consistent and
356 random; then, the correlation between elevation measurements derived from different satellites could be
357 analyzed with the probability distributions of elevation difference values between the elevation
358 measurements and the base DEM. Specifically, we calculated the elevation difference values using either
359 the SRTM DEM or ASTER DEM as the base DEM and for both the stable and glacier regions. According



360 to the probability distribution curves shown in Fig. 5 (a), the elevation measurements of the ASTER
 361 DEM were strongly correlated with the ICESat data-derived elevation measurements in the stable region,
 362 and both showed slight positive biases compared with those of the SRTM DEM data. We analyzed the
 363 correlation between different satellite measurements in the glacier region, as shown in Fig. 5 (c). The
 364 elevation measurements between ICESat and CryoSat-2 were strongly correlated, and the elevation
 365 measurements of ICESat, ICESat-2 and CryoSat-2 were greater than those of the ASTER DEM. We
 366 found that the elevation measurements of ICESat-2 were the smallest both in the stable region and in the
 367 glacier region. We linked this situation to the observation scale of the satellite sensors, meaning that the
 368 spatial resolution of the derived ASTER DEM was 30 m, and the footprint diameters of ICESat, ICESat-
 369 2 and CryoSat-2 were 70 m, 17.5 m, and 300 m, respectively. Among these satellites, ICESat-2 had the
 370 finest spatial observation scale. We compared the elevation measurements of the stable region with those
 371 of the glacier region. According to Fig. 5 (b) and (c), the precisions of the elevation measurements
 372 obtained by satellite sensors were different between the stable region and glacier region, indicating that
 373 the elevation measurements from the ASTER DEM were more consistent with the altimetry data in the
 374 stable region; this difference may be mainly due to the relatively flat terrain in the stable region.





(c)

Figure 5: Cross analysis of multisource satellite measurements. The histograms are probability distributions of elevation difference values derived by satellite measurement and the DEM image. The colors of histograms are corresponding to different satellite data sources. In addition, the elevation difference values are obtained from the stable region and the glacier region, respectively.

375 The ICESat-2 satellite carries ATLAS, which features new technologies that enable it to collect more
376 detailed and precise elevation measurements of the Earth's surface. The ICESat-2 collects the
377 measurements by emitting pairwise beams, and each beam pair consists of a strong and a weak beam.
378 For the CryoSat-2 swath altimetry data, which were also mentioned as CryoTEMPO-EOLIS point data
379 in our study, swath processing fully exploits the information contained in CryoSat-2 waveforms and
380 leads to one to two orders of magnitude more measurements than the CryoSat-2 L2 data processed by
381 the point-of-closest-approach (POCA) technique. Accordingly, we evaluated the performance of the
382 strong beam and weak beam measurements of the ICESat-2 data, as well as the CryoSat-2 swath and L2
383 measurements of the CryoSat-2 data in this study. We calculated the elevation difference between the
384 ICESat-2 data and the ASTER DEM in the stable region, as shown in Fig. 6 (a). The ICESat-2 strong
385 beam and weak beam had no significant differences in elevation measurements. CryoSat-2 swath and L2
386 measurements were taken on the glacier region. According to Fig. 6 (b), the CryoSat-2 swath
387 measurements were relatively consistent with the ASTER DEM measurements, while the CryoSat-2 L2
388 measurements showed large differences from the ASTER DEM measurements. Accordingly, we can
389 conclude that the CryoSat-2 swath data achieve significant improvement over the CryoSat-2 L2 data in
390 terms of glacier elevation measurements.

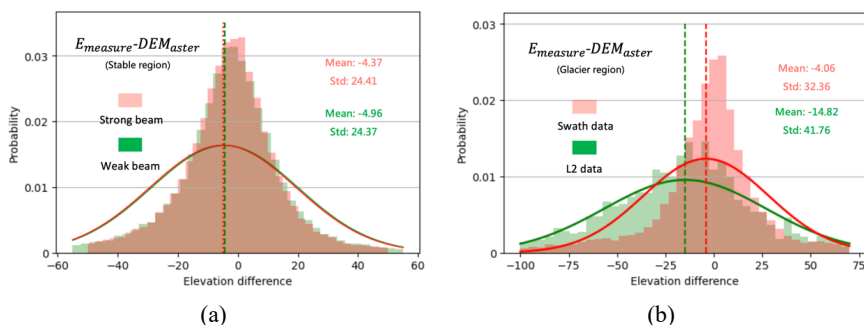


Figure 6: Comparisons of homologous elevation measurements. The elevation difference is calculated using the elevation measurements and ASTER DEM image. (a) Probability distribution histograms of elevation



differences for the ICESat-2 strong beam measurements and weak beam measurements. (b) Probability distribution histograms of elevation differences for the CryoSat-2 swath measurements and CryoSat-2 L2 measurements.

391 **5.2 Comparison of existing estimates of glacier elevation change**

392 Many researchers have exploited the rate of glacier elevation change in the SETP region, which is similar
393 to the region of the Nyainqentanglha range or the Hengduan Mountains (Gardner et al., 2013; Neckel et
394 al., 2014; Yi et al., 2020; Shean et al., 2020). According to the estimates shown in Fig. 7 (a), studies
395 show large disparities among the estimated glacier elevation change rates, and the largest and smallest
396 negative elevation changes correspond to -1.34 m/yr and -0.4 m/yr, respectively (Kääb et al., 2015;
397 Gardner et al., 2013). Among the 16 collected estimates of glacier elevation change rates, 12 estimates
398 ranged from -0.9 m/yr to -0.5 m/yr. Our estimates also fell within this scope and were consistent with the
399 recent research by Hugonnet et al. (2021); specifically, the rates of glacier elevation change for 2000-
400 2012, 2012-2022, and 2000-2022 were -0.58 ± 0.05 m/yr, -0.78 ± 0.04 m/yr, and -0.71 ± 0.05
401 m/yr, respectively, which were similar to the estimates of -0.55 ± 0.28 m/yr, -0.81 ± 0.41 m/yr,
402 and -0.69 ± 0.35 m/yr for the periods 2000-2009, 2010-2019, and 2000-2019, respectively, by
403 Hugonnet et al. (2021). Our estimate for the period of 2000-2022 was also very similar to the estimates
404 of Zhao et al. (2022) and Brun et al. (2017), who demonstrated that glaciers melted at rates of $-0.71 \pm$
405 0.18 m/yr and -0.73 ± 0.27 m/yr during the periods of 2000-2019 and 2000-2016, respectively.

406 To accurately capture accurate glacier elevation changes, different satellite data sources have been
407 explored for quantifying glacier elevation changes in recent studies. The ICESat data have been widely
408 used for estimating the rate of glacier elevation change for the period of 2003-2009, as shown in Fig. 7.
409 (b) The rates of glacier elevation change derived from ICESat data have great disparities (Gardner et al.,
410 2013; Neckel et al., 2014; Kääb et al., 2015). The CryoSat-2 interferometric-swath-processed data, which
411 were recently applied for estimation of the rate of glacier elevation change, are estimated for the period
412 of 2011-2019 to be -1.15 ± 0.12 m/yr (Jakob et al., 2021), which seems to indicate a slightly more
413 rapid rate of glacier thinning than other studies. The estimates obtained from time-series ASTER DEMs
414 seem to fall within a reasonable range between -0.55 m/yr and -0.81 m/yr (Hugonnet et al., 2021 and
415 Brun et al., 2017). Generally, among the single data source-based estimates of glacier elevation change



416 rates, the ASTER DEM-derived results exhibited high consistency, while the ICESat data-derived results
417 varied greatly. We believe that this difference is mainly due to the spatially continuous observation of
418 the ASTER stereo images, which provide more abundant elevation measurements than the dispersed
419 observation of the ICESat data and thus result in more robust estimates. With the increase in accessible
420 satellite data, additional satellite data have been integrated to improve the estimation of glacier elevation
421 change rates. Multisource data integration can enhance glacier observations at both spatial and temporal
422 scales and reduce bias caused by anomalous measurements from single-source data. We integrated the
423 ICESat, ICESat-2, and ASTER DEMs and CryoSat-2 data and achieved improved estimates of the rate
424 of glacier elevation change with wider temporal coverage and lower uncertainty. More accessible satellite
425 data can be combined for the estimation of glacier elevation changes, and we believe that a high-
426 efficiency combination strategy and improved satellite data processing technique will be crucial factors
427 for future improved estimations.

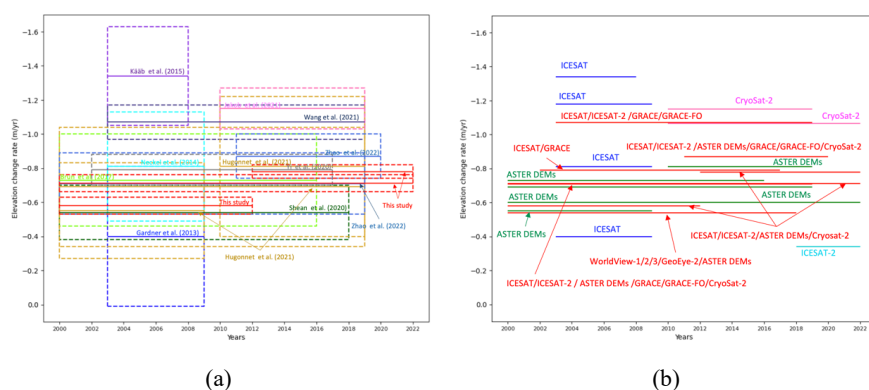


Figure 7: Estimates of glacier elevation change rate in published studies. (a) The glacier elevation change rates with estimate uncertainties and (b) the data source for the estimation of glacier elevation change rate.

428 6. Conclusion

429 We integrate multisource satellite data (including ASTER DEM, ICESat GLAH14, ICESat-2 ATL06,
430 and CryoSat-2 CryoTEMPO-EOLIS point data) to estimate the glacier elevation changes across the
431 entire SETP region over the past two decades. We found that glaciers are experiencing rapid and
432 heterogeneous elevation thinning in the SETP, and the mean glacier thinning rate is $-0.710 \pm$



433 0.046 *m/yr*. In particular, the glacier thinning rates for the periods 2000-2012 and 2012-2022 were
434 estimated, and we found that the glacier thinning rate in the recent decade of 2012-2022 accelerated by
435 31.2% compared with that in the previous period of 2000-2012.

436 The estimates for individual glaciers show large disparities; that is, the proportions of accumulating
437 glaciers, moderate melting glaciers and rapid melting glaciers account for 12.6%, 56.5%, and 30.9%,
438 respectively. We compared the newly accessible CryoSat-2 swath data with the CryoSat-2 L2 data and
439 found that the elevation measurements from the CryoSat-2 swath data agreed significantly more with the
440 elevation measurements from other satellite observations. According to extensive cross-analyses of
441 glacier elevation measurements derived from different satellite sources, we found that the glacier
442 elevation measurements derived from the new advanced ICESat-2 satellite were slightly smaller than
443 those derived from other satellite observations. Among the existing studies on the estimates of glacier
444 elevation changes in the SETP region, our estimates are highly consistent with recent studies and have
445 higher temporal resolution and lower estimate uncertainty.

446 **Code/Data availability**

447 The ICESat GLAH and ICESat-2 ATL06 used in this study are available from the National Snow and
448 Ice Data Center (NSIDC). The CryoSat-2 CryoTEMPO-EOLIS point data were obtained from
449 <https://cryotempo-eolis.org>. The aster stereo images were acquired at
450 <https://search.earthdata.nasa.gov/search>. The datasets generated in this study are available from the
451 authors upon request. The processing code is available at [https://github.com/xinluo2018/Glacier-in-](https://github.com/xinluo2018/Glacier-in-SETP)
452 SETP.

453 **Author contributions**

454 Xin Luo developed the methods and wrote the paper. Hongping Zeng and Zhen Ye assisted with the
455 data processing.

456 **Competing interests**

457 The authors declare that they have no conflicts of interest.



458 **Acknowledgments**

459 This work is supported by the National Natural Science Foundation of China (Proj No. 42001351).

460 Sentinel-1 SAR images were obtained from the European Space Agency.

461

462 **References**

463 Arendt, A., Bliss, A., Bolch, T., Cogley, J. G., Gardner, A., Hagen, J. O., Zheltyhina, N.: Randolph
464 Glacier inventory—a dataset of global glacier outlines: Version 6.0: Technical report, global land ice
465 measurements from space, 2017.

466 Bach, E., Radić, V., Schoof, C.: How sensitive are mountain glaciers to climate change? Insights from a
467 block model, *J. Glaciol.*, 64, 247–258, 2018.

468 Beyer, Ross, A., Oleg, A., Scott, M.: The Ames Stereo Pipeline: NASA's open source software for
469 deriving and processing terrain data, *E.S.S.*, 5, 2018.

470 Bhushan, S., Shean, D., Alexandrov, O., and Henderson, S.: Automated digital elevation model (DEM)
471 generation from very-high-resolution Planet SkySat triplet stereo and video imagery, *ISPRS J.*
472 *Photogram. Remote Sens.*, 173: 151-165, 2021.

473 Bhattacharya, A, Mukherjee, K., King, O., Karmaker, S., Remya, S.N., Kulkarni, A. V., and Kropáček,
474 J., Bolch, T.: Influence of climate and non-climatic attributes on declining glacier mass budget and
475 surging in Alaknanda Basin and its surroundings, *Glob. Planet. Chang.*, 230: 104260, 2023.

476 Brunt, K.M., Neumann, T. A., Smith, B. E.: Assessment of ICESat-2 ice sheet surface heights, based on
477 comparisons over the interior of the Antarctic ice sheet, *G.R.L.*, 46 (22): 13072-13078, 2019.

478 Bolch, T., Buchroithner, M.F., Peters, J., Baessler, M., Bajracharya, S.: Identification of glacier motion
479 and potentially dangerous glacial lakes in the Mt. Everest region/Nepal using spaceborne imagery, *Nat.*
480 *Hazards Earth Syst. Sci.*, 8, 1329–1340, 2008.

481 Brun, F., Berthier, E., Wagnon, P.: A spatially resolved estimate of High Mountain Asia glacier mass
482 balances from 2000 to 2016, *Nat. Geosci.*, 10 (9): 668-673, 2017.

483 Barundun, M., Huss, M., Sold, L., Farinotti, D., Azisov, E., Salzmann, N.: Re-analysis of seasonal mass
484 balance at Abramov glacier 1968–2014, *J. Glaciol.*, 61, 1103–1117, 2015.



-
- 485 Carrivick, J.L, Tweed, F.S.: A global assessment of the societal impacts of glacier outburst floods, *Glob.*
486 *Planet. Chang.*, 144, 1–16, 2016.
- 487 Chen, J., Chen, J., Liao, A.: Global land cover mapping at 30 m resolution: A POK-based operational
488 approach, *ISPRS J. Photogram. Remote Sens.*, 103: 7-27, 2015.
- 489 Chen, X., Long, D., Hong, Y., Zeng, C., Yan, D.H.: Improved modeling of snow and glacier melting by
490 a progressive two-stage calibration strategy with GRACE and multisource data: how snow and glacier
491 meltwater contributes to the runoff of the Upper Brahmaputra River basin? *Water Resour. Res.*, 53, 2431–
492 2466, 2017.
- 493 Cogley, J. G., Hock, R., Rasmussen, L. A., Arendt, A. A., Bauder, A., Braithwaite, R. J., Jansson, P.,
494 Kaser, G., Möller, M., Nicholson, L., and Zemp, M.: Glossary of glacier mass balance and related terms,
495 IHP-VII Technical Documents in Hydrology 1045 No. 86, IACS Contribution No. 2, Organization,
496 UNESCO-IHP, Paris, France, 2011.
- 497 Farr, T.G., Rosen, P.A., Caro, E., Crippen, R., Duren, R., Hensley, S., Kobrick, M., Paller, M.,
498 Rodriguez, E., Roth, L., Seal, D., Shaffer, S., Shimada, J., Umland, J., Werner, M., Oskin, M.,
499 Burbank, D., Alsdorf, D.: The shuttle radar topography mission. *Rev. Geophys.*, 45, Rg2004, 2007.
- 500 Fricker, H. A., Borsa, A., Minster, B.: Assessment of ICESat performance at the salar de Uyuni, Bolivia.,
501 *Geophys. Res. Lett.*, 32 (21), 2005.
- 502 Gardner, A.S., Moholdt, G., Cogley, J.G.: A reconciled estimate of glacier contributions to sea level rise:
503 2003 to 2009, *Sci.*, 340 (6134): 852-857, 2013.
- 504 Ghuffar, S., Bolch, T., Rupnik, E., and Bhattacharya, A.: A pipeline for automated processing of
505 declassified Corona KH-4 (1962–1972) stereo imagery, *IEEE Trans. Geosci. Remote Sens.*, 2022, 60: 1-
506 14.
- 507 Guan, W., Cao, B., Pan, B.: Updated Surge-Type Glacier Inventory in the West Kunlun Mountains,
508 Tibetan Plateau, and Implications for Glacier Change, *J. Geophys. Res. Earth Surf.*, 2022, 127 (1):
509 e2021JF006369, 2022.
- 510 Goumelen, N., Escorihuela, M.J., Shepherd, A.: CryoSat-2 swath interferometric altimetry for mapping
511 ice elevation and elevation change, *Adv. Space Res.*, 62 (6): 1226-1242, 2018.
- 512 Hu, H., Chen, C., Wu, B., Yang, X., Zhu, Q., Yulin Ding, Y.: Texture-aware dense image matching using



-
- 513 ternary census transform. *ISPRS Annals of Photogramm, Remote Sens. Spatial Inf. Sci*, 3, 59–66, 2016.
- 514 Hugonnet, R., McNabb, R., Berthier, E.: Accelerated global glacier mass loss in the early twenty-first
515 century, *Nat.*, 592 (7856): 726–731, 2021.
- 516 Hirschmuller, H.: Stereo processing by semiglobal matching and mutual information, *IEEE Trans.*
517 *Pattern Anal. Mach. Intell.*, 30, 328–341, 2008.
- 518 Mairi, D.: IPCC’s special report on the ocean and cryosphere in a changing climate: what’s in it for South
519 Asia? 2020.
- 520 Jacob, T., Wahr, J., Pfeffer, T.W.: Swenson, S. Recent contributions of glaciers and ice caps to sea level
521 rise, *Nat.*, 482, 514, 2012.
- 522 Jakob, L., Gourmelen, N., Ewart, M.: Plummer, S. Spatially and temporally resolved ice loss in High
523 Mountain Asia and the Gulf of Alaska observed by CryoSat-2 swath altimetry between 2010 and 2019,
524 *The Cryosphere*, 15, 1845–1862, 2021.
- 525 Kääb, A., Berthier, E., Nuth, C., Gardelle, J., Arnaud, Y.: Contrasting patterns of early twenty-first-
526 century glacier mass change in the Himalayas, *Nature*, 488(7412): 495–498, 2012.
- 527 Kääb, A., Treichler, D., Nuth, C., Berthier, E.: Contending estimates of 2003–2008 glacier mass balance
528 over the Pamir–Karakoram–Himalaya, *The Cryosphere*, 9, 557–564, 2015.
- 529 Ke, L., Ding, X., Song, C.: Heterogeneous changes of glaciers over the western Kunlun Mountains based
530 on ICESat and Landsat-8 derived glacier inventory, *Remote Sens. Environ.*, 168: 13–23, 2015.
- 531 Ke, L., Song, C., Yong, B.: Which heterogeneous glacier melting patterns can be robustly observed from
532 space? A multi-scale assessment in southeastern Tibetan Plateau, *Remote Sens. Environ.*, 242: 111777,
533 2020.
- 534 King, O., Ghuffar, S., Bhattacharya, A., Yao, R., Yao, T. and Bolch, T.: Glaciological and climatological
535 drivers of heterogeneous glacier mass loss in the Tanggula Shan (Central-Eastern Tibetan Plateau), since
536 the 1960s, *J. Glaciol.*, 1–18, 2023.
- 537 Muhammad, S., Tian, L.: Mass balance and a glacier surge of Guliya ice cap in the western Kunlun Shan
538 between 2005 and 2015, *Remote Sens. Environ.*, 244: 111832, 2020.
- 539 Milner, A.M., Khamis, K., Battin, T.J., Brittain, J.E., Barrand, N.E., Füreder, L., CauvyFraunié, S.,
540 Gislason, G.M., Jacobsen, D., Hannah, D.M., Hodson, A.J., Hood, E., Lencioni, V., Ólafsson, J.S.,



-
- 541 Robinson, C.T., Tranter, M., Brown, L.E.: Glacier shrinkage driving global changes in downstream
542 systems, *Proc. Natl. Acad. Sci. U. S. A.*, 114, 9770–9778, 2017.
- 543 Robson, B. A., Bolch, T., MacDonell, S., Hölbling, D., Rastner, P., Schaffer, N.: Automated detection of
544 rock glaciers using deep learning and object-based image analysis, *Remote Sens. Environ.*, 250: 112033,
545 2020.
- 546 NASA/METI/AIST/Japan SpaceSystems and U.S./Japan ASTER Science Team: ASTER Level 1A Data
547 Set - Reconstructed, Unprocessed Instrument Data. NASA EOSDIS Land Processes DAAC. Accessed
548 2021-01-15 from, 2001.
- 549 Neckel, N., Kropáček, J., Bolch, T., Hochschild, V.: Glacier mass changes on the Tibetan Plateau 2003–
550 2009 derived from ICESat laser altimetry measurements, *Environ. Res. Lett.*, 9, 014009, 2014.
- 551 Nuth, C., Kääb, A.: Co-registration and bias corrections of satellite elevation datasets for quantifying
552 glacier thickness change, *The Cryosphere*, 5, 271–290, 2011.
- 553 Piermattei, L., Zemp, M., Sommer, C., Brun, F., Braun, M. H., Andreassen, L. M., Belart, J. M. C.,
554 Berthier, E., Bhattacharya, A., Boehm Vock, L., Bolch, T., Dehecq, A., Dussailant, I., Falaschi, D.,
555 Florentine, C., Floricioiu, D., Ginzler, C., Guillet, G., Hugonnet, R., Huss, M., Kääb, A., King, O., Klug,
556 C., Knuth, F., Krieger, L., La Frenierre, J., McNabb, R., McNeil, C., Prinz, R., Sass, L., Seehaus, T.,
557 Shean, D., Treichler, D., Wendt, A., and Yang, R.: Observing glacier elevation changes from spaceborne
558 optical and radar sensors – an inter-comparison experiment using ASTER and TanDEM-X data,
559 *EGUsphere [preprint]*, <https://doi.org/10.5194/egusphere-2023-2309>, 2023.
- 560 Pope, A., Rees, W. G.: Impact of spatial, spectral, and radiometric properties of multispectral imagers on
561 glacier surface classification, *Remote Sens. Environ.*, 141: 1-13. 2014.
- 562 Prefecture, M.B.O.N.: *Meteorological Chronicle of Nyingchi Prefecture, Tibet*, Sichuan Science and
563 Technology Press, Sichuan, 2014.
- 564 Peng, Y, He J, Yuan, Q, Wang, S., Chu, X., Zhang, L.: Automated glacier extraction using a Transformer
565 based deep learning approach from multi-sensor remote sensing imagery, *ISPRS J. Photogram. Remote*
566 *Sens.*, 202: 303-313, 2023.
- 567 Pekel, J.F., Cottam, A., Gorelick, N.: High-resolution mapping of global surface water and its long-term
568 changes, *Nat.*, 540 (7633): 418-422, 2016.



-
- 569 Robson, B. A., MacDonell, S., Ayala, Á., Bolch, T., Nielsen, P. R., and Vivero, S.: Glacier and rock
570 glacier changes since the 1950s in the La Laguna catchment, Chile, *The Cryosphere*, 16, 647–665,
571 <https://doi.org/10.5194/tc-16-647-2022>, 2022.
- 572 Sakai, A., Nuimura, T., Fujita, K., Takenaka, S., Nagai, H., Lamsal, D., Climate regime of Asian glaciers
573 revealed by GAMDAM glacier inventory, *The Cryosphere*, 9, 865–880, 2015.
- 574 Smith, B., Fricker, H.A., Gardner, A., Siegfried, M.R., Adusumilli, S., Csatho, B.M., Holschuh, N.,
575 Nilsson, J., Paolo, F.S.: the ICESat-2 Science Team, ATLAS/ICESat-2 L3A Land Ice Height,
576 Version 1, NASA National Snow and Ice Data Center Distributed Active Archive Center, Boulder,
577 Colorado USA, 2020.
- 578 Shean, D.E., Alexandrov, O., Moratto, Z.M., Smith, B. E., Joughin, I. R., Porter, C., Morin, P.: An
579 automated, open-source pipeline for mass production of digital elevation models (DEMs) from very high-
580 resolution commercial stereo satellite imagery, *ISPRS J. Photogram. Remote Sens.*, 116, 2016.
- 581 Shean, D.E., Bhushan, S., Montesano, P.: A systematic, regional assessment of high mountain Asia
582 glacier mass balance. *Front. Earth Sc-switz.*, 2020, 7: 363, 2020.
- 583 Smith, B., Fricker, H.A., Gardner, A., Siegfried, M.R., Adusumilli, S., Csatho, B.M., Holschuh, N.,
584 Nilsson, J., Paolo, F.S.: the ICESat-2 Science Team, ATLAS/ ICESat-2 L3A Land Ice Height, Version
585 1, NASA National Snow and Ice Data Center Distributed Active Archive Center, Boulder, Colorado
586 USA, 2020.
- 587 Treichler, D. and Kaab, A.: ICESat laser altimetry over small mountain glaciers, *The Cryosphere*, 10,
588 2129–2146, 2016.
- 589 Wang, X., Liu, L., Hu, Y.: Multi-decadal geomorphic changes of a low-angle valley glacier in the East
590 Kunlun Mountains: remote sensing observations and detachment hazard assessment, *Nat Hazard. Earth*
591 *Sys.*, 2021, 21 (9): 2791-2810, 2021.
- 592 Yao, T., Thompson, L., Yang, W., Yu, W., Gao, Y., Guo, X., Yang, X., Duan, K., Zhao, H., Xu, B., Pu,
593 J., Lu, A., Xiang, Y., Kattel, D.B., Joswiak, D.: Different glacier status with atmospheric circulations in
594 Tibetan Plateau and surroundings, *Nat. Clim. Chang.*, 2, 663–667, 2012.
- 595 Yi, S., Song, C.Q., Heki, K., Kang, S.C., Wang, Q.Y., Chang, L.: Satellite-observed monthly glacier and
596 snow mass changes in Southeast Tibet: implication for substantial meltwater contribution to the



- 597 Brahmaputra, *The Cryosphere*, 14, 2267–2281, 2020.
- 598 Zhao, F., Long, D., Li, X.: Rapid glacier mass loss in the Southeastern Tibetan Plateau since the year
599 2000 from satellite observations, *Remote Sens. Environ.*, 270: 112853, 2022.
- 600 Zhou, C., Zheng, L.: Mapping radar glacier zones and dry snow line in the Antarctic Peninsula using
601 Sentinel-1 images, *Remote Sens.*, 9: 1171, 2017.
- 602 Zwally, H. J., Schutz, B., Abdalati, W.: ICESat's laser measurements of polar ice, atmosphere, ocean,
603 and land. *J. Geodyn.*, 34 (3-4): 405-445, 2002.
- 604 Zwally, H.J., Schutz, R., Hancock, D., Dimarzio, J.: GLAS/ICESat L2 Global Land Surface
605 Altimetry Data (HDF5), Version 34, NASA National Snow and Ice Data Center Distributed Active
606 Archive Center, Boulder, Colorado USA, 2014.
- 607